


Reconstruction of attosecond beating by interference of two-photon transitions on the lithium atom with Rabi oscillations

Yijie Liao ¹, Yueming Zhou ^{1,*}, Liang-Wen Pi,^{2,3,†} Jintai Liang,¹ Qinghua Ke,¹ Yong Zhao,¹ Min Li ¹ and Peixiang Lu^{1,4}

¹*School of Physics and Wuhan National Laboratory for Optoelectronics, Huazhong University of Science and Technology, Wuhan 430074, China*

²*State Key Laboratory of Transient Optics and Photonics, Xi'an Institute of Optics and Precision Mechanics of the Chinese Academy of Sciences, Xi'an 710119, China*

³*University of Chinese Academy of Science, Beijing 100049, China*

⁴*Optics Valley Laboratory, Hubei 430074, China*

 (Received 30 December 2021; revised 16 March 2022; accepted 16 June 2022; published 24 June 2022)

We present numerical simulations of the reconstruction of attosecond beating by interference of two-photon transitions (RABBITT) on lithium by solving the three-dimensional time-dependent Schrödinger equation. In our scheme, the infrared (IR) field couples the $2s$ and $2p$ states of lithium and leads to the Rabi oscillations of populations between these two states. We analyzed the RABBITT phases of the two peaks in the Rabi-oscillation-induced Autler-Townes splittings. Our results show that the relative phase between these two peaks changes with the photoelectron energy and depends on the intensity of the IR field. Moreover, in the angle-resolved RABBITT measurement, the phases of the two peaks depend differently on the emission angle of photoelectrons. These behaviors are traced back to the different initial phases of the electron wave packets emitted from the dressed $2p$ states and the competition among different ionization channels.

DOI: [10.1103/PhysRevA.105.063110](https://doi.org/10.1103/PhysRevA.105.063110)

I. INTRODUCTION

The advent of attosecond extreme ultraviolet (XUV) pulses [1,2] paved the way towards monitoring the electronic motion on the attosecond time scale. The reconstruction of attosecond beating by interference of two-photon transitions (RABBITT) technique [3] utilizing the attosecond pulses is widely employed to investigate the electronic dynamics in atoms [4–6], molecules [7–9], solids [10,11], and liquids [12]. In the RABBITT measurements, an XUV attosecond pulse train (APT) synchronized with a weak time-delayed infrared (IR) field ionizes a target through the two-photon transitions [13,14]. Owing to the interference between the ionized electron wave packets generated by different two-photon channels, the photoelectron yield of sidebands (SBs) located between the main peaks oscillates with the time delay between the XUV and IR fields. From the oscillation of the SB signals, the relative phase of the outgoing electron wave packets can be retrieved, which contains two contributions, the phase of the XUV harmonics and the atomic phase. So, the RABBITT technique has been used to characterize the XUV APT [15–17] and to reconstruct the atomic phase.

The atomic phase encodes the electronic dynamics in photoionization [18]. It is related to the structure of the electron wave packet and the target potential landscape witnessed by the escaping electrons. In the absence of resonances [19], the ionized electron wave packet is unstructured, and the atomic

phase can be approximately divided into the two phases corresponding to the bound-free transition and the free-free transition (the continuum-continuum transition) [20], the energy derivatives of which are the Wigner time delay [21,22] and the continuum-continuum time delay [23–25], respectively. In the case of the two-photon transition through a resonance [26], the electron wave packet is structured, resulting in the rapid phase variation of the emitted electron wave packet within a narrow energy range near the resonance [27,28]. The modification on the phase of the electron wave packet by the resonance has been demonstrated in the cases of Fano resonances [29–33], shape resonances [34,35], and giant resonances [36–38]. In addition, the sudden phase jumps of the ejected electron wave packet have also been revealed when the laser field is resonant with the atomic bound level in the RABBITT measurement [39–44]. Beyond that, the polarization of the target ionic state also leads to an additional term in the phase of the outgoing electron wave packet, which has been investigated in the photoemission of polar molecules [45] and in the shake-up ionization of helium [46–48] with the angle-resolved photoelectron spectroscopy [40–42,48–52].

In the previous RABBITT schemes, the modulation on the phase of the ejected electron wave packet is induced by the special structure of the target. On the other hand, a laser field could steer the structure of the states and thus may modulate the phase of the outgoing electron wave packet. For example, the IR field could induce Rabi oscillations [53] between two atomic bound levels. The superposition of the two coupled states forms the structured state. Rabi oscillation leads to Autler-Townes (AT) splittings [54] in the photoelectron energy spectra, which can be understood as the formation of

*zhouymhust@hust.edu.cn

†lwpi@opt.ac.cn

a doublet of dressed quasienergy states [55] separated by the energy spacing of the Rabi frequency Ω_R . The electrons ionized from the dressed states carry different phases. It is worthwhile to elucidate how the process of Rabi oscillations of the structured state modulates the phase of the ionized electron wave packet. We notice that recently the interference of the photoelectrons from the dressed states has been studied by inspecting the asymmetry of the AT doublet [56].

In this paper, we study the influence of Rabi oscillations on the phase of the ionized electron wave packet using the RABBITT technique. In a recent study [42], the modification of the photoelectron spectrum of lithium when the $2s$ - $2p$ transition is resonant with the IR field of the RABBITT scheme has been shown. It revealed that the resonance changed entirely the ionization dynamics and modified the obtained RABBITT phases. However, due to short pulse duration of the IR field, and broad spectral width of the XUV field, Rabi oscillations and AT splittings were not observed there. In our paper we employ the IR field with much longer pulse duration and thus multiple cycles of Rabi oscillations occur. Owing to narrow spectral widths of both the XUV and IR fields, the AT splittings are resolvable in SBs of the photoelectron energy spectra. We separately analyzed the oscillations in the signals for the two peaks of the SB splittings as a function of the time delay. Our results show that the RABBITT phases are different between these two peaks of the doublet in the angle-integrated spectra, and this difference varies with the photoelectron energy and depends on the intensity of the IR field. In the angle-resolved RABBITT measurement, abrupt jumps appear in the retrieved phases. Interestingly, the angle dependences of the RABBITT phases are different between the two peaks of the doublet and their angle dependences change with the photoelectron energy and rely on the IR intensity. These different phase behaviors between the two peaks of the doublet are traced back to the unequal initial phases of the electron wave packets generated from the dressed $2p$ states, which stem from the out-of-phase oscillations in the $2p$ population relative to the $2s$ -population oscillations. Moreover, the details in these different phase behaviors between the two peaks of the doublet reveal the competition among different ionization channels.

This paper is structured as follows. In Sec. II, we introduce the numerical methods in our calculations, including numerically solving the three-dimensional (3D) time-dependent Schrödinger equation (TDSE) (Sec. II A) and the calculation of the ionization amplitudes within the perturbation framework (Sec. II B). Sections III and IV show the numerical results in the angle-integrated and angle-resolved RABBITT measurements, respectively. We finish with a summary in Sec. V. Atomic units are used throughout this paper unless otherwise stated.

II. METHODS

A. Numerically solving the three-dimensional time-dependent Schrödinger equation

To uncover the effects of Rabi oscillations on the phase of the ejected wave packet, we solve the 3D TDSE for the lithium atom, which has a single electron outside a closed shell.

Thus, the single-active-electron (SAE) model is reasonable to describe the photoionization of lithium. Within the SAE approximation, the TDSE in velocity gauge is written as

$$i \frac{\partial \Psi(\mathbf{r}, t)}{\partial t} = \left[\frac{\mathbf{p}^2}{2} + \mathbf{A}(t) \cdot \mathbf{p} + V(\mathbf{r}) \right] \Psi(\mathbf{r}, t), \quad (1)$$

where $V(\mathbf{r})$ is the effective one-electron potential of lithium adopted from Ref. [57]. The external laser field is described as

$$\mathbf{A}(t) = [A_{\text{IR}}(t) + A_{\text{XUV}}(t; \tau)] \hat{z}, \quad (2)$$

where $A_{\text{IR}}(t)$ and $A_{\text{XUV}}(t; \tau)$ are the vector potentials of the IR and XUV fields, respectively. τ is the time delay between the two laser fields. The IR field is expressed as

$$A_{\text{IR}}(t) = A_0 \cos^2 \left(\frac{\pi t}{2\tau_{\text{IR}}} \right) \sin(\omega t), \quad (3)$$

where A_0 is the amplitude of the IR vector potential. $\omega = 0.0614$ a.u. and $T = 2\pi/\omega$ are the frequency and the period of the IR field, respectively. Here $\tau_{\text{IR}} = 160T$ determines the duration of the IR field, corresponding to a spectral width of 0.023 eV. The time-delayed XUV field is modeled as

$$A_{\text{XUV}}(t; \tau) = \sum_{n=-120}^{120} (-1)^n A_n \exp \left[-2 \ln 2 \frac{(t + \tau - nT/2)^2}{\tau_{\text{XUV}}^2} \right] \times \sin[\omega_{\text{XUV}}(t + \tau - nT/2)], \quad (4)$$

where

$$A_n = A_{n0} \exp \left[-2 \ln 2 \frac{(nT/2)^2}{\tau_{\text{APT}}^2} \right]. \quad (5)$$

Here A_{n0} is the amplitude of the XUV vector potential and $\omega_{\text{XUV}} = 15\omega$ is the central frequency of the XUV field. $\tau_{\text{XUV}} = 0.08T$ and $\tau_{\text{APT}} = 50T$ determine the durations of the XUV pulse and the APT, respectively. The spectral width of the XUV field is 0.021 eV.

The wave function of the TDSE is expanded as a partial wave series

$$\Psi(\mathbf{r}, t) = \sum_{l=0}^{L_{\text{max}}} \sum_{m=-l}^l \frac{R_{lm}(r, t)}{r} Y_{lm}(\theta, \phi), \quad (6)$$

where R_{lm} is the radial part of the wave function. $Y_{lm}(\theta, \phi)$ denotes the spherical harmonics, where θ and ϕ are the polar angle and the azimuthal angle, respectively. l and m are the angular momentum quantum number and the magnetic quantum number, respectively.

In our calculations, $m = 0$ due to the XUV and IR fields are both linearly polarized along the \hat{z} axis and $L_{\text{max}} = 30$ ensures convergence. R_{lm} is discretized by the finite-element discrete variable representation method [58], where the box size is $R_{\text{max}} = 280$ a.u. The initial state is calculated by imaginary-time propagation, which yields the ionization potentials of $I_p^{2s} = 0.1978$ a.u., $I_p^{2p} = 0.1364$ a.u., and $I_p^{3s} = 0.0802$ a.u. for the $2s$, $2p$, and $3s$ states of lithium, respectively. Note that in this model the energy spacing between the $2s$ and $2p$ levels is 1.67 eV. It deviates from the experimental value given in NIST by the amount of 0.18 eV. The time propagation of the TDSE is implemented by the split-Lanczos method [59] with the time step $\Delta t = 0.02$ a.u. In

the each-step propagation, we apply an absorbing mask function, $F(r) = 1 - 1/[1 + e^{(150.0-r)/2.0}]$, which splits the wave function $\Psi(\mathbf{r}, t)$ into the inner part $\Psi_{\text{in}}(\mathbf{r}, t) = F(r)\Psi(\mathbf{r}, t)$ and the outer part $\Psi_{\text{out}}(\mathbf{r}, t) = [1 - F(r)]\Psi(\mathbf{r}, t)$. The inner part $\Psi_{\text{in}}(\mathbf{r}, t)$ evolves as Eq. (1) and the outer part $\Psi_{\text{out}}(\mathbf{r}, t)$ is propagated by the Coulomb-Volkov propagator [60]. The ionization amplitudes are obtained by projecting the outer part $\Psi_{\text{out}}(\mathbf{r}, t)$ on the set of Volkov states.

B. Perturbative treatment of the ionization amplitudes

In the previous RABBITT scheme, the ionization from the initial state is directly treated with the lowest-order perturbation theory (LOPT) [18,19,61]. In our RABBITT scheme, because the IR field $E_{\text{IR}}(t)$ is resonantly tuned to the transition between the $2s$ ($|\psi_{2s}\rangle$) and $2p$ ($|\psi_{2p}\rangle$) states of lithium, the Rabi oscillations happen, which is beyond the perturbation scheme, and thus the previous treatment is not valid. To provide an intuitive physical picture we modified the previous LOPT calculations, where we separately treat the Rabi oscillations and the ionization as follows [56,62,63].

The Rabi oscillation between the $2s$ and $2p$ levels is described by the Rabi model [53]. The resulting wave function is expressed as

$$|\psi_n\rangle = \cos\left(\frac{\Omega_{\text{R}}t}{2}\right)e^{-i\omega_{2s}t}|\psi_{2s}\rangle - i\sin\left(\frac{\Omega_{\text{R}}t}{2}\right)e^{-i\omega_{2p}t}|\psi_{2p}\rangle, \quad (7)$$

where ω_{2s} and ω_{2p} are the energies of $|\psi_{2s}\rangle$ and $|\psi_{2p}\rangle$, respectively. $\Omega_{\text{R}} = E_0 f_{\text{IR}}(t)|\langle\psi_{2p}|z|\psi_{2s}\rangle|$ is the Rabi frequency. Here E_0 and $f_{\text{IR}}(t)$ are the amplitude and the envelope of the electric field, respectively. In our LOPT calculations, the wave function $|\psi_n\rangle$ of Eq. (7) is regarded as the zeroth-order solution of our RABBITT scheme. Thus the zeroth-order amplitude $a_n^{(0)}(t)$ is written as [56,63,64]

$$a_n^{(0)}(t) = \cos\left(\frac{\Omega_{\text{R}}t}{2}\right)\delta_{n,2s} - i\sin\left(\frac{\Omega_{\text{R}}t}{2}\right)\delta_{n,2p}. \quad (8)$$

Then, the ionization in the RABBITT scheme is handled with the LOPT. The N th-order amplitude $a_m^{(N)}(t)$, which

describes the N -photon transition to state $|\psi_m\rangle$, can be derived from the $(N-1)$ th-order amplitude as [65]

$$a_m^{(N)}(t) = \frac{1}{i} \sum_{\nu} \int_{-\infty}^t dt' e^{i\omega_{m\nu}t'} V_{m\nu}(t') a_{\nu}^{(N-1)}(t'), \quad (9)$$

where $\omega_{m\nu} \equiv \omega_m - \omega_{\nu}$ is the transition frequency between the states $|\psi_{\nu}\rangle$ and $|\psi_m\rangle$. The term $V_{m\nu}(t) = -\boldsymbol{\mu}_{m\nu} \cdot \mathbf{E}(t) = E(t)\langle\psi_m|z|\psi_{\nu}\rangle$ describes the time-dependent perturbation of the system by the linearly polarized external field $\mathbf{E}(t) = \hat{z}E(t)$, where $\boldsymbol{\mu}_{m\nu}$ is the transition dipole moment between $|\psi_{\nu}\rangle$ and $|\psi_m\rangle$.

Using the Fourier transform $\tilde{E}(\omega) = \int_{-\infty}^{\infty} E(t)e^{i\omega t} dt$ and the recurrence relation in Eq. (9), the one-photon ionization amplitude is obtained as

$$\begin{aligned} \lim_{t \rightarrow \infty} a_f^{(1)}(t) &= \frac{1}{2i} \langle\psi_f|z|\psi_{2s}\rangle \tilde{E}\left(\omega_f - \omega_{2s} + \frac{\Omega_{\text{R}}}{2}; \tau\right) \\ &+ \frac{1}{2i} \langle\psi_f|z|\psi_{2s}\rangle \tilde{E}\left(\omega_f - \omega_{2s} - \frac{\Omega_{\text{R}}}{2}; \tau\right) \\ &- \frac{1}{2i} \langle\psi_f|z|\psi_{2p}\rangle \tilde{E}\left(\omega_f - \omega_{2p} + \frac{\Omega_{\text{R}}}{2}; \tau\right) \\ &+ \frac{1}{2i} \langle\psi_f|z|\psi_{2p}\rangle \tilde{E}\left(\omega_f - \omega_{2p} - \frac{\Omega_{\text{R}}}{2}; \tau\right). \end{aligned} \quad (10)$$

It describes the one-photon transition from the initial state $|\psi_n\rangle$ to the continuum state $|\psi_f\rangle$ by absorbing a photon Ω from the field $\mathbf{E}(t; \tau)$, where the energy-preserving condition $\Omega = \omega_f - \omega_{2s,2p} \pm \frac{\Omega_{\text{R}}}{2}$ is satisfied. Here we take $t \rightarrow \infty$ because the photoelectrons are measured long after the interaction with the field is over. Note that the Fourier transform of the time-delayed field is $\tilde{E}(\Omega; \tau) = e^{-i\Omega\tau} \tilde{E}(\Omega)$ [26].

Likewise, the two-photon ionization amplitude from the initial state $|\psi_n\rangle$ to the continuum state $|\psi_f\rangle$ via the intermediate state $|\psi_{\nu}\rangle$ is given as

$$\begin{aligned} \lim_{t \rightarrow \infty} a_f^{(2)}(t) &= \frac{1}{2i} \int_{-\infty}^{\infty} d\Omega_1 \tilde{E}_1(\Omega_1; \tau) \tilde{E}_2(\omega_f - \omega_{2s} + \frac{\Omega_{\text{R}}}{2} - \Omega_1) \sum_{\nu} \frac{\langle\psi_f|z|\psi_{\nu}\rangle \langle\psi_{\nu}|z|\psi_{2s}\rangle}{\omega_{2s} - \frac{\Omega_{\text{R}}}{2} + \Omega_1 - \omega_{\nu}} \\ &+ \frac{1}{2i} \int_{-\infty}^{\infty} d\Omega_1 \tilde{E}_1(\Omega_1; \tau) \tilde{E}_2(\omega_f - \omega_{2s} - \frac{\Omega_{\text{R}}}{2} - \Omega_1) \sum_{\nu} \frac{\langle\psi_f|z|\psi_{\nu}\rangle \langle\psi_{\nu}|z|\psi_{2s}\rangle}{\omega_{2s} + \frac{\Omega_{\text{R}}}{2} + \Omega_1 - \omega_{\nu}} \\ &- \frac{1}{2i} \int_{-\infty}^{\infty} d\Omega_1 \tilde{E}_1(\Omega_1; \tau) \tilde{E}_2(\omega_f - \omega_{2p} + \frac{\Omega_{\text{R}}}{2} - \Omega_1) \sum_{\nu} \frac{\langle\psi_f|z|\psi_{\nu}\rangle \langle\psi_{\nu}|z|\psi_{2p}\rangle}{\omega_{2p} - \frac{\Omega_{\text{R}}}{2} + \Omega_1 - \omega_{\nu}} \\ &+ \frac{1}{2i} \int_{-\infty}^{\infty} d\Omega_1 \tilde{E}_1(\Omega_1; \tau) \tilde{E}_2(\omega_f - \omega_{2p} - \frac{\Omega_{\text{R}}}{2} - \Omega_1) \sum_{\nu} \frac{\langle\psi_f|z|\psi_{\nu}\rangle \langle\psi_{\nu}|z|\psi_{2p}\rangle}{\omega_{2p} + \frac{\Omega_{\text{R}}}{2} + \Omega_1 - \omega_{\nu}}. \end{aligned} \quad (11)$$

It describes the two-photon transition through the absorption of a photon Ω_1 from the field $\mathbf{E}_1(t; \tau)$ followed by the absorption of a photon ω_2 from the field $\mathbf{E}_2(t)$, where the energy-preserving condition $\omega_2 = \omega_f - \omega_{2s,2p} \pm \frac{\Omega_{\text{R}}}{2} - \Omega_1$ is satisfied. For the two-photon transition involving the emission of a photon, the ionization amplitude has a similar

form as Eq. (11), but the corresponding photon frequency is negative.

Equations (10) and (11) indicate that the ionization from the initial superposition state $|\psi_n\rangle$ can be understood to start from the dressed quasienergy states of $|\psi_{2s}\rangle$ and $|\psi_{2p}\rangle$. More specifically, the first and second lines in Eqs. (10) and (11)

correspond to the dressed $2s$ states $|\phi_{2s}^l\rangle$ and $|\phi_{2s}^h\rangle$ with the quasienergies of $\omega_{2s} - \frac{\Omega_R}{2}$ and $\omega_{2s} + \frac{\Omega_R}{2}$, respectively. The third and fourth lines in Eqs. (10) and (11) are associated to the dressed $2p$ states $|\phi_{2p}^l\rangle$ and $|\phi_{2p}^h\rangle$ with the quasienergies of $\omega_{2p} - \frac{\Omega_R}{2}$ and $\omega_{2p} + \frac{\Omega_R}{2}$, respectively. Note that there is a minus at the beginning of the third line in Eq. (11), which means that the initial phase of the electron wave packet generated from $|\phi_{2p}^l\rangle$ has an additional term of π , compared to that for $|\phi_{2p}^h\rangle$. The different initial phases between the dressed $2p$ states stem from the out-of-phase Rabi oscillations in the $2p$ population with respect to the $2s$ -population oscillations, as indicated by Eq. (7).

In our calculations, the XUV and IR fields are both spectrally narrow enough and display no spectral overlap. Therefore, each term in Eqs. (10) and (11) can be approximately calculated by multiplying the corresponding electric-field amplitude to the residual integration of wave functions. Here the integration of wave functions can be further divided into the angular and radial parts. For the two-photon transition amplitudes in Eq. (11), the infinite summation in the radial part is evaluated with the Dalgarno-Lewis method [66]. Then the radial part can be calculated using the perturbed wave functions [67,68], which satisfy the inhomogeneous equation and the boundary conditions described in Refs. [69,70]. Particularly, the integration of two continuum wave functions appearing in Eq. (11) is calculated by using a complex coordinate rotation method [71].

III. ANGLE-INTEGRATED RABBITT PHASES

Figure 1(a) displays the angle-integrated photoelectron energy spectra as a function of the time delay between the XUV and IR fields, obtained by solving the 3D TDSE. Here the intensities of the XUV and IR fields are 1×10^{13} and 1×10^{11} W/cm², respectively. The frequency of the IR field is 0.0614 a.u., which is resonant with the $2s$ - $2p$ transition. One of the most intriguing features in Fig. 1(a) is the splittings of the main peaks and SBs in the photoelectron energy spectra. The splittings in Fig. 1(a) are induced by the Rabi oscillations of the populations between the bound states of lithium. This Rabi oscillation can be intuitively seen by projecting the time-dependent TDSE solution to the field-free eigenstates at the zero values of the vector potential of the field, which approximately indicates the population evolution of the $2s$ and $2p$ states [72], as shown in Fig. 1(b). Here, the population of the $3s$ state is also shown because the frequency of the IR field is also very close to the $2p$ - $3s$ transition frequency. As shown in Fig. 1(b), the out-of-phase oscillations of the $2s$ and $2p$ populations are drastic while very little population is leaked to the $3s$ state. This Rabi oscillation leads to the splitting of the $2s$, $2p$, and $3s$ states and thus the AT splitting in the energy spectrum. In the following, the lower- and higher-energy peaks of the AT splitting in each SB are denoted as P^l and P^h , respectively.

As shown in Fig. 1(a), the photoelectron yields of the two peaks P^h and P^l of the doublet in each SB oscillate in different phases with the time delay τ between the XUV and IR fields. To reveal this difference, we compare the τ dependence of the photoelectron yields for P^h and P^l in Figs. 1(c) and 1(d).

For SB 10 [Fig. 1(c)], the relative RABBITT phase between the two peaks is close to π . For SB 16 [Fig. 1(d)], there is a noticeable shift as compared to SB 10.

The oscillations of the doublets P^h and P^l in SBs originate from the interference among different ionization channels. As an example, we display the dominant ionization pathways contributing to P^h with the photoelectron energy of $2q\omega - I_p^{2s} + \frac{\Omega_R}{2}$ in Fig. 1(e). As described in Sec. II B, in our RABBITT scheme, the $2s$ and $2p$ states are both populated during Rabi oscillations, thus photoelectrons are ejected from both the $2s$ and $2p$ states [56]. There are two pathways initiated from $|\phi_{2s}^h\rangle$. Pathways 1 and 2 denote the absorption of one XUV harmonic photon (Ω_{2q-1} or Ω_{2q+1}) followed by the exchange of one IR photon ω . Pathway 3 indicates the transition from $|\phi_{2p}^h\rangle$ to the final state SB_{2q} , through the absorption of one harmonic photon Ω_{2q-1} . Note that, because the IR-induced transition from $2s$ to $2p$ has already been included in treating the Rabi oscillations, the resonant two-photon pathway ($|\phi_{2s}^h\rangle \rightarrow |\phi_{2p}^h\rangle \rightarrow SB_{2q}$) [42] is excluded from the perturbative treatment here [56]. Because the $3s$ state ($|\psi_{3s}\rangle$) can also be populated with our IR field, two more pathways initiated from the dressed $3s$ state ($|\phi_{3s}^h\rangle$) contribute to P^h , denoted as pathways 4 and 5 in Fig. 1(e). However, the population in the $3s$ state is very low [as shown in Fig. 1(b)], especially when the intensity of the IR field decreases, as shown in Fig. 2. So, the contributions of pathways 4 and 5 are relatively small.

We extract the RABBITT phase from P^l and P^h in each SB of the angle-integrated photoelectron energy spectra, by fitting the 2ω oscillations of the SB signals with $S_{2q}^{2\omega} = \beta \cos(2\omega\tau - \phi)$ after being frequency filtered by a Fourier transform [8,73]. Figures 3(a) and 3(b) respectively show the RABBITT phases ϕ^l and ϕ^h for the lower- (P^l) and higher-energy peaks (P^h) as a function of the photoelectron energy. As displayed in Fig. 3(a), the energy dependence of ϕ^l relies on the IR intensity. For the IR intensities of 1×10^{10} and 3×10^{10} W/cm², ϕ^l shows nearly no change with the photoelectron energy. For the IR intensity of 1×10^{11} W/cm², ϕ^l increases with the photoelectron energy. For P^h , the phases ϕ^h show an increasing trend with the photoelectron energy for the three IR intensities, as shown in Fig. 3(b).

To reveal these discrepancies more clearly, we display the relative phase $\Delta\phi = \phi^h - \phi^l$ as a function of the photoelectron energy in Fig. 3(c). For the IR intensities of 1×10^{10} and 3×10^{10} W/cm², $\Delta\phi$ is close to π . As the photoelectron energy increases, $\Delta\phi$ decreases from SB 10 to SB 14 and then increases at SB 16, as shown in Fig. 3(c). For the IR intensity of 1×10^{11} W/cm², $\Delta\phi$ decreases with the photoelectron energy and it deviates more from π as the photoelectron energy increases.

In the following, we illuminate how the channel competition affects $\Delta\phi$. According to Eqs. (10) and (11), the ionization amplitudes for pathways 1 to 3 can be separately written as

$$A_L^{(1)}(E_{\pm}) = \frac{1}{2i} \tilde{E}_{\text{XUV}}(\Omega_{2q-1}) \tilde{E}_{\text{IR}}(\omega) e^{-i\Omega_{2q-1}\tau + i\phi_{2q-1}} \times \sum_v \frac{\langle \psi_f | z | \psi_v \rangle \langle \psi_v | z | \psi_{2s} \rangle}{\omega_{2s} \pm \frac{\Omega_R}{2} + \Omega_{2q-1} - \omega_v}, \quad (12a)$$

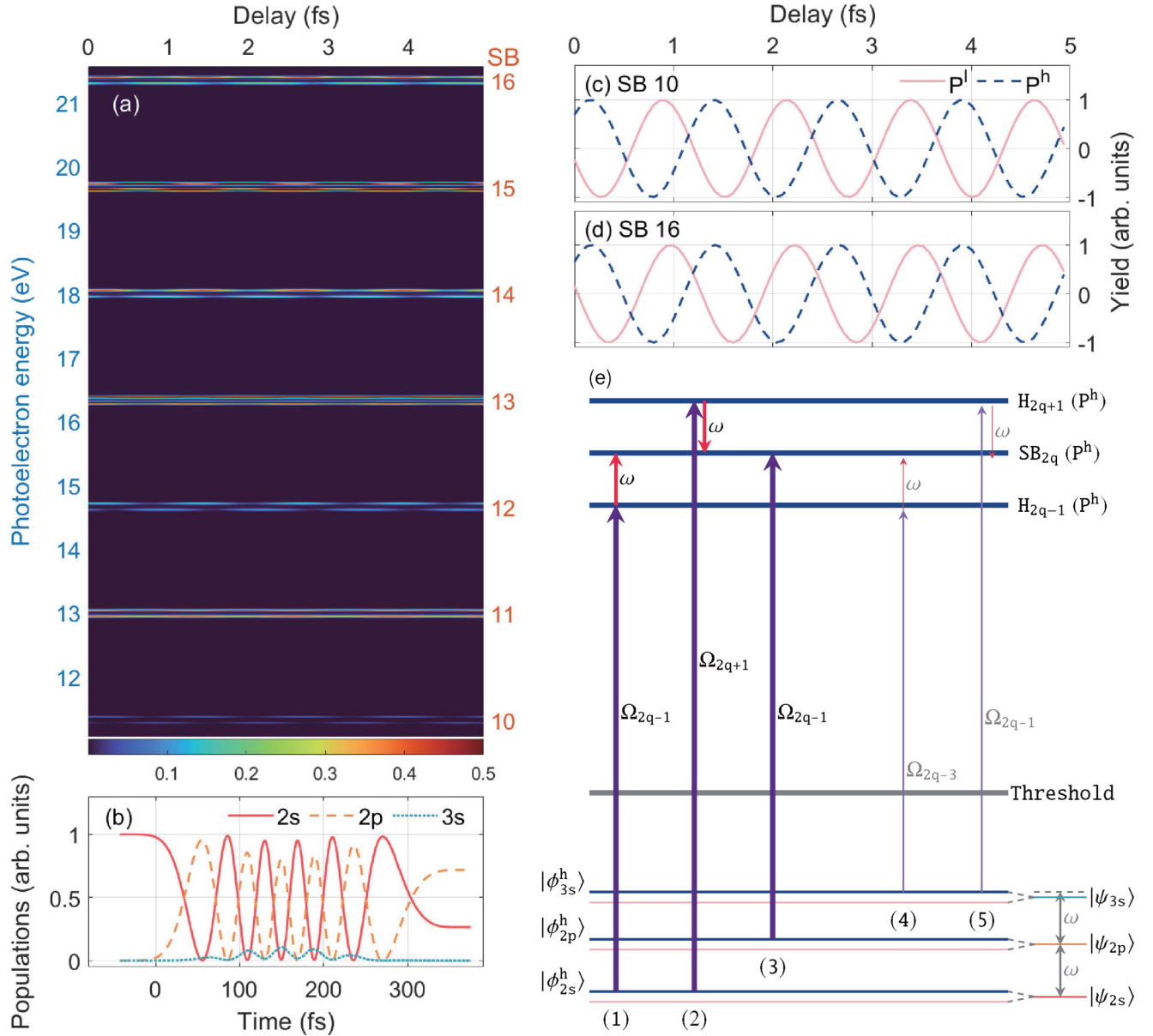


FIG. 1. (a) The angle-integrated photoelectron energy spectra as a function of the time delay between the XUV and IR fields, where the intensities of the XUV and IR fields are 1×10^{13} and 1×10^{11} W/cm², respectively. The corresponding energy spacing between the AT splittings is 0.0034 a.u. (b) The populations of the 2s (red solid line), 2p (orange dashed line), and 3s (green dotted line) states of lithium as a function of the atom-field interaction time. (c) The normalized 2ω oscillations for the two peaks of the doublet in SB 10, which are obtained by the Fourier transform. The pink-solid and blue-dashed lines correspond to P^l and P^h , respectively. (d) The same as (c), but for SB 16. (e) The ionization pathways for P^h with the photoelectron energy of $2q\omega - I_p^{2s} + \frac{\Omega_R}{2}$.

$$A_L^{(2)}(E_{\pm}) = \frac{1}{2i} \tilde{E}_{XUV}(\Omega_{2q+1}) \tilde{E}_{IR}(-\omega) e^{-i\Omega_{2q+1}\tau + i\phi_{2q+1}} \times \sum_v \frac{\langle \psi_f | z | \psi_v \rangle \langle \psi_v | z | \psi_{2s} \rangle}{\omega_{2s} \pm \frac{\Omega_R}{2} + \Omega_{2q+1} - \omega_v}, \quad (12b)$$

$$A_L^{(3)}(E_{\pm}) = \pm \frac{1}{2i} \tilde{E}_{XUV}(\Omega_{2q-1}) e^{-i\Omega_{2q-1}\tau + i\phi_{2q-1}} \langle \psi_f | z | \psi_{2p} \rangle, \quad (12c)$$

where $L = 0, 2$ is the angular momentum of the final scattering state $|\psi_f\rangle$ [74]. $E_{\pm} = 2q\omega - I_p^{2s} \pm \frac{\Omega_R}{2}$ is the energy of $|\psi_f\rangle$ related to the doublet P^h and P^l , respectively. Approximately, the continuum-continuum (CC) phase is inde-

pendent of the angular momentum L [19]. Hence, the phases of the transition amplitudes for pathways 1 to 3 can be separately expressed as

$$\arg A_L^{(1)}(E_{\pm}) = -\Omega_{2q-1}\tau + \phi_{2q-1} + \varphi^{(1)}(E_{\pm}), \quad (13a)$$

$$\arg A_L^{(2)}(E_{\pm}) = -\Omega_{2q+1}\tau + \phi_{2q+1} + \varphi^{(2)}(E_{\pm}), \quad (13b)$$

$$\arg A_L^{(3)}(E_{\pm}) = -\Omega_{2q-1}\tau + \phi_{2q-1} + \varphi_L^{(3)}(E_{\pm}), \quad (13c)$$

where $\phi_{2q\pm 1}$ are the phases of the corresponding XUV harmonics. Here $\varphi^{(i)}(E_{\pm})$ and $\varphi_L^{(i)}(E_{\pm})$ are the atomic phases of pathway i for the doublet P^h and P^l . The subscript of $\varphi_L^{(3)}$ denotes the L dependence of these atomic phases. The atomic

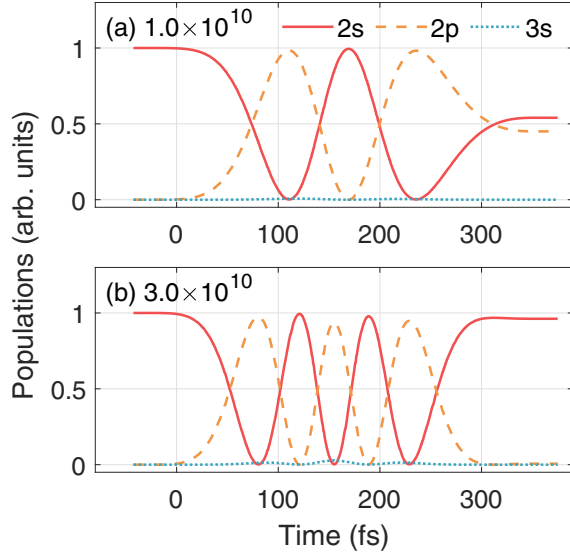


FIG. 2. The populations of the $2s$ (red-solid lines), $2p$ (orange-dashed lines), and $3s$ (green-dotted lines) states of lithium as a function of the atom-field interaction time. The intensities of the IR field are (a) 1×10^{10} (corresponding to the energy spacing of 0.0012 a.u.) and (b) 3×10^{10} W/cm² (corresponding to the energy spacing of 0.0020 a.u.).

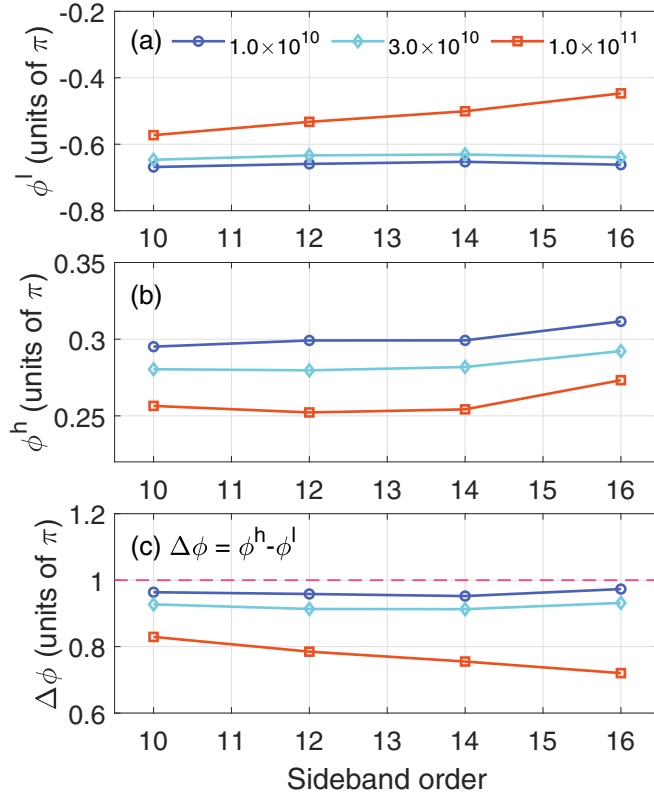


FIG. 3. (a) The angle-integrated RABBITT phases for P^l as a function of the photoelectron energy. (b) The same as (a), but for P^h . (c) The relative phases between P^l and P^h , as a function of the photoelectron energy. The purple circles, blue rhombuses, and orange squares correspond to the IR intensities of 1×10^{10} , 3×10^{10} , and 1×10^{11} W/cm², respectively.

phases of pathways 1 to 3 are separately given as

$$\varphi^{(1)}(E_{\pm}) = \eta_{\lambda}^{(+)}(E_{\pm}) + \varphi_{\text{CC}}^{(+)}(E_{\pm}) - \lambda\pi/2 + \pi, \quad (14a)$$

$$\varphi^{(2)}(E_{\pm}) = \eta_{\lambda}^{(-)}(E_{\pm}) + \varphi_{\text{CC}}^{(-)}(E_{\pm}) - \lambda\pi/2 + \pi, \quad (14b)$$

$$\varphi_L^{(3)}(E_{\pm}) = \eta_L(E_{\pm}) - L\pi/2 \mp \pi/2, \quad (14c)$$

where η_L and $\eta_{\lambda}^{(\pm)}$ represent the scattering phases and $\varphi_{\text{CC}}^{(\pm)}$ denotes the CC phases [19]. The superscripts (\pm) refer to the absorption or emission of the IR photon. Here $\lambda = 1$ is the angular momentum of the intermediate state $|\psi_{\nu}\rangle$.

Due to the subtle energy spacing between P^h and P^l (Ω_R), the scattering phases and the CC phases in Eq. (14) are nearly the same for the two peaks of each doublet, i.e., $\eta_L(E_+) = \eta_L(E_-)$, $\eta_{\lambda}^{(\pm)}(E_+) = \eta_{\lambda}^{(\pm)}(E_-)$, and $\varphi_{\text{CC}}^{(\pm)}(E_+) = \varphi_{\text{CC}}^{(\pm)}(E_-)$. Hence, the atomic phases of pathways 1 and 2 are the same for the two peaks of the doublet, i.e., $\varphi^{(1)}(E_+) = \varphi^{(1)}(E_-)$ and $\varphi^{(2)}(E_+) = \varphi^{(2)}(E_-)$. However, the atomic phases of pathway 3 [$\varphi_L^{(3)}(E_{\pm})$] are different between the two peaks of each doublet due to the existence of $\mp\pi/2$ in the last term of Eq. (14c). This π difference between $\varphi_L^{(3)}(E_+)$ and $\varphi_L^{(3)}(E_-)$ stems from the different initial phases of the dressed $2p$ states, as indicated by Eq. (10).

The 2ω oscillations in the angle-integrated SB signals originate from the interference of pathway 2 with pathways 1 and 3. The RABBITT phase ϕ , retrieved from the 2ω oscillations in the SB signals, contains the relative XUV harmonics phase $\Delta\phi_{2q} = \phi_{2q+1} - \phi_{2q-1}$ and the relative atomic phase of the interfering pathways. In our calculations, $\Delta\phi_{2q}$ equals to π for the two peaks of the doublet in all of the SBs [Eq. (4)]. Therefore, the RABBITT phase due to the interference between pathway 2 and pathway 1 is the same for the doublet P^h and P^l . However, for the interference between pathways 2 and 3, the relative RABBITT phase $\Delta\phi$ between the two peaks of the doublet is π , which equals to the difference between $\varphi_L^{(3)}(E_+)$ and $\varphi_L^{(3)}(E_-)$. Actually, the relative phases $\Delta\phi$ shown in Fig. 3(c) are neither zero nor π , revealing the competition between pathways 1 and 3.

We calculate the relative ionization contributions $|\mathcal{A}^{(i)}|/|\mathcal{A}_{\text{tot}}|$ for the doublet P^h and P^l in all of the SBs. Here $\mathcal{A}^{(i)}$ is the ionization amplitude of pathway i and \mathcal{A}_{tot} is the total ionization amplitude. Figure 4 displays the results for the three IR intensities. The top and bottom rows in Fig. 4 correspond to P^h and P^l , respectively. Owing to the subtle energy spacing between the doublet P^h and P^l , the relative contributions of each pathway are nearly the same for the two peaks of the doublet. At low photoelectron energies, the contributions of the $3s$ state (pathways 4 and 5) are small, thus we only consider the interference among pathways 1 to 3 for simplicity. As shown in Fig. 4, for the SBs 10 to 14, pathway 3 dominates over pathway 1 for the three IR intensities. This dominance results in the approximate π value of $\Delta\phi$ for the SBs 10 to 14 at all of the three IR intensities in Fig. 3(c). As the IR intensity increases, pathway 3 is less dominant over pathway 1. This explains why $\Delta\phi$ for the SBs 10 to 14 departs more from π as the IR intensity increases, as shown in Fig. 3(c). At each IR intensity, the dominance of pathway 3 over pathway 1 decreases with the photoelectron energy for the SBs 10 to 14. Accordingly, as the photoelectron energy increases, $\Delta\phi$ at each IR intensity deviates more from

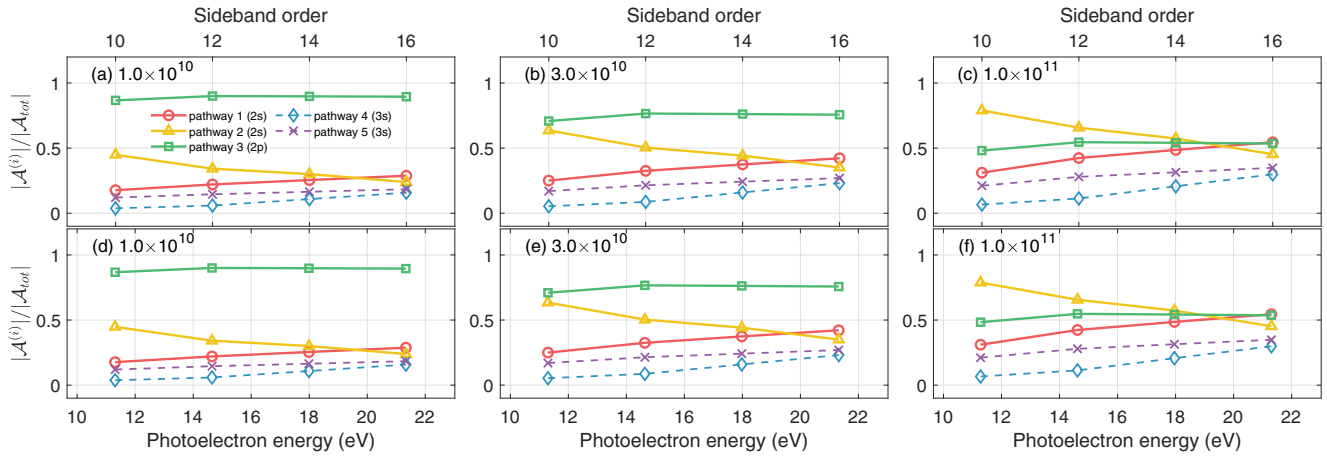


FIG. 4. From left to right: The relative contributions from different pathways as a function of the photoelectron energy, for the IR intensities of (a), (d) 1×10^{10} , (b), (e) 3×10^{10} , and (c), (f) 1×10^{11} W/cm². The top (a)–(c) and bottom (d)–(f) rows correspond to P^h and P^l , respectively. The red circles, yellow triangles, green squares, blue rhombuses, and purple crosses correspond to pathways 1, 2, 3, 4, and 5, respectively.

π for the SBs 10 to 14 in Fig. 3(c). In addition, the ionization contribution of the $3s$ state rises with the photoelectron energy and these contributions are non-negligible for the SBs with higher photoelectron energies, which also modifies the energy dependence of $\Delta\phi$ for SB 16 in Fig. 3(c).

IV. ANGLE-RESOLVED RABBITT PHASES

Figure 5 shows the RABBITT phases as a function of the emission angle θ of photoelectrons. Here the angle-resolved phases are plotted relative to the polarization direction $\theta = 0$. The top and bottom rows display the results for the doublets P^l and P^h , respectively. The angle dependences of the RABBITT phases are different between P^l and P^h . For P^l , as shown in Figs. 5(a)–5(c), there is only one phase jump around $\theta = 60^\circ$ for the SBs 10 to 14, while for SB 16 two phase jumps

successively occur at $\theta < 60^\circ$ and $\theta = 80^\circ$. For P^h , as shown in Figs. 5(d)–5(f), only one phase jump occurs near $\theta = 65^\circ$ for all of the SBs.

It has been demonstrated in previous studies that the phase jumps originate from the interference between different partial waves [40–42,48–51,75]. In our case, the s and d partial waves can be generated through three pathways because the populations are transferred among the $2s$ and $2p$ states. Figure 4 has shown that the relative contributions of different pathways are identical for the two peaks of the doublet, and they depend on the IR intensity and the photoelectron energy. Furthermore, our calculations show that the relative contributions of the two partial waves in each pathway are also identical for the two peaks of the doublet and they are independent of the IR intensity. As a demonstration, Fig. 6 shows the amplitude ratios of the d wave to the s wave ($|A_2^{(d)}|/|A_0^{(i)}|$) for P^h , as a function

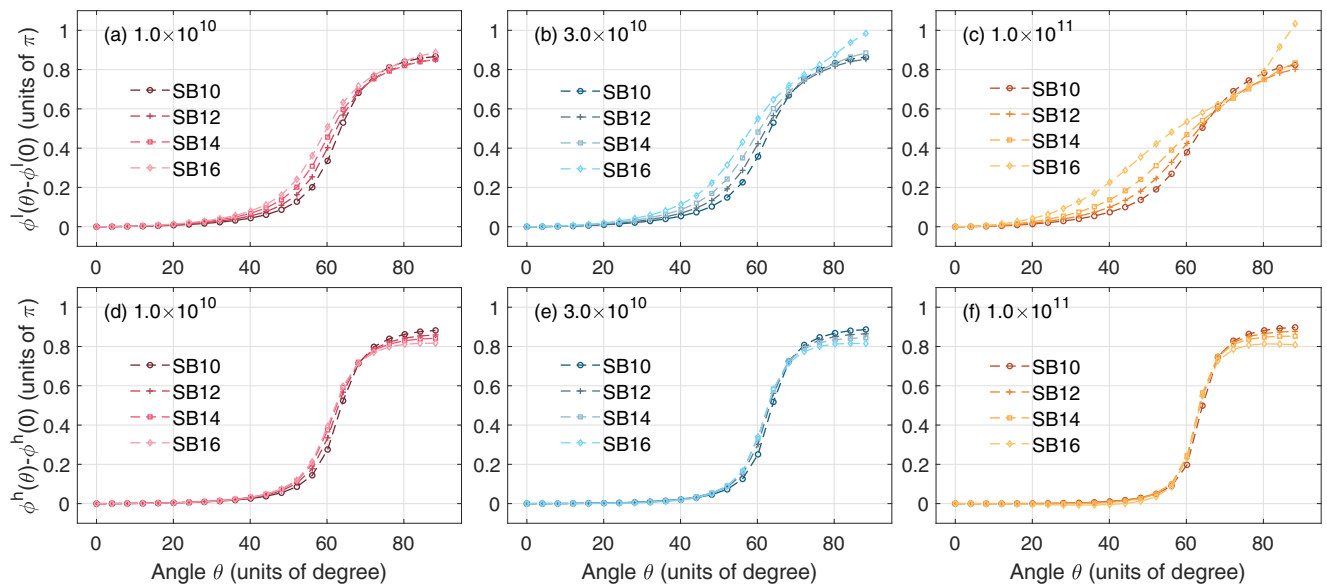


FIG. 5. From left to right: The angle-resolved RABBITT phases (relative to the polarization direction) as a function of the emission angle of photoelectrons, for the IR intensities of (a), (d) 1×10^{10} , (b), (e) 3×10^{10} , and (c), (f) 1×10^{11} W/cm². The top (a)–(c) and bottom (d)–(f) rows correspond to P^l and P^h , respectively. The circles, pluses, squares, and rhombuses correspond to SBs 10, 12, 14, and 16, respectively.

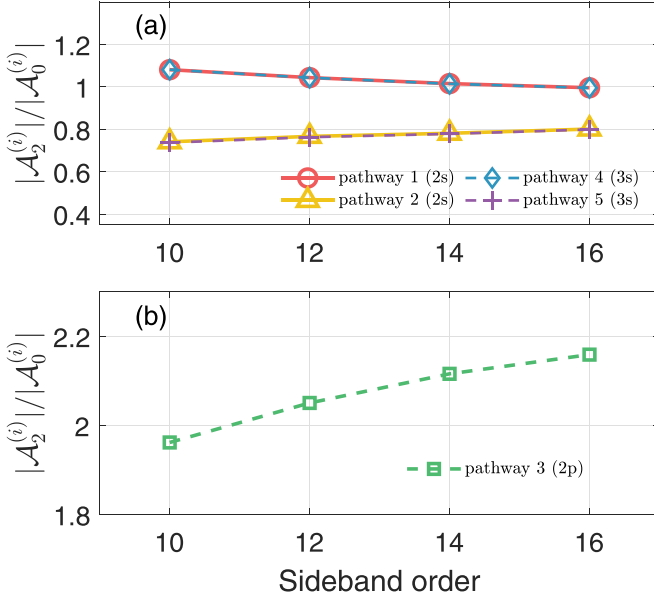


FIG. 6. (a) The amplitude ratios of the d -wave channel to the s -wave channel for pathways 1 (red circles), 2 (yellow triangles), 4 (blue rhombuses), and 5 (purple pluses), as a function of the photoelectron energy. (b) The same as (a), but for pathway 3 (green squares).

of the photoelectron energy. Here $\mathcal{A}_2^{(i)}$ and $\mathcal{A}_0^{(i)}$ are the amplitudes for pathway i as given in Eq. (12). Figure 6(a) shows the ratios for the two-photon pathways through the continuum intermediate state. It shows that the energy dependence of these ratios relies on whether the IR photon is absorbed (pathways 1 and 4) or emitted (pathways 2 and 5), which is consistent with the results in Refs. [25,75,76]. As shown in Fig. 6(b), in pathway 3, the d wave dominates over the s wave for all of the SBs, which coincides with the Fano propensity rule [77].

In the following, we analyze the origin of the phase jumps shown in Fig. 5. For simplicity, we only consider pathways 1 to 3 for the SBs with lower photoelectron energies (the SBs 10 to 14), owing to the small ionization contribution from pathways 4 and 5 and the little population in the $3s$ state. In the LOPT [19], the angle-resolved SB signal for the doublet P^h and P^l can be described as

$$P_{2q}(E_{\pm}, \theta, \tau) = 2\pi \left| \sum_{L=0,2} Y_L^0(\theta) \times [\mathcal{A}_L^{(1)}(E_{\pm}) + \mathcal{A}_L^{(2)}(E_{\pm}) + \mathcal{A}_L^{(3)}(E_{\pm})] \right|^2, \quad (15)$$

where $E_{\pm} = 2q\omega - I_p^{2s} \pm \frac{\Omega_R}{2}$ is the photoelectron energy related to P^h and P^l , respectively. The 2ω oscillation of the angle-resolved SB signal is written as

$$P_{2q}^{2\omega}(E_{\pm}, \theta, \tau) = \mathcal{B}(E_{\pm}, \theta) \cos[2\omega\tau - \Delta\phi_{2q} - \varphi^{(2)}(E_{\pm}) + \varphi^{(1)}(E_{\pm})] + \mathcal{C}(E_{\pm}, \theta) \cos[2\omega\tau - \Delta\phi_{2q} - \varphi^{(2)}(E_{\pm}) + \varphi_0^{(3)}(E_{\pm})] + \mathcal{D}(E_{\pm}, \theta) \cos[2\omega\tau - \Delta\phi_{2q} - \varphi^{(2)}(E_{\pm}) + \varphi_2^{(3)}(E_{\pm})], \quad (16)$$

where $\varphi^{(i)}$ and $\varphi_L^{(i)}$ are the atomic phases of pathway i and they are given in Eq. (14). Here $\Delta\phi_{2q} = \pi$ is the relative phase between the neighboring XUV harmonics, which is identical for the two peaks of the doublet in all of the SBs [Eq. (4)]. The three 2ω -oscillation components in Eq. (16) separately describe the partial-wave interference of pathway 2 with pathways 1 and 3. The coefficients of these three 2ω -oscillation components are expressed as

$$\mathcal{B}(E_{\pm}, \theta) = 4\pi(Y_0^0)^2 |\mathcal{A}_0^{(2)}| |\mathcal{A}_0^{(1)}| \times [1 + ab(Y_2^0/Y_0^0)^2 + (a+b)(Y_2^0/Y_0^0)], \quad (17a)$$

$$\mathcal{C}(E_{\pm}, \theta) = 4\pi(Y_0^0)^2 |\mathcal{A}_0^{(2)}| |\mathcal{A}_0^{(3)}| [1 + b(Y_2^0/Y_0^0)], \quad (17b)$$

$$\mathcal{D}(E_{\pm}, \theta) = 4\pi(Y_2^0)^2 |\mathcal{A}_2^{(2)}| |\mathcal{A}_2^{(3)}| [1 + b^{-1}(Y_0^0/Y_2^0)], \quad (17c)$$

where $a = |\mathcal{A}_2^{(1)}|/|\mathcal{A}_0^{(1)}|$ and $b = |\mathcal{A}_2^{(2)}|/|\mathcal{A}_0^{(2)}|$. The coefficients $\mathcal{B}(E_{\pm}, \theta)$, $\mathcal{C}(E_{\pm}, \theta)$, and $\mathcal{D}(E_{\pm}, \theta)$ are determined by the magnitudes of the partial waves in different pathways. Because the competition among the pathways varies with the IR intensity (Fig. 4), the values of these coefficients depend on the IR intensity.

As explained in previous studies [48,49,75], the phase jump occurs near the angle where the amplitude of $P_{2q}^{2\omega}$ changes sign. In our case, for the SBs 10 to 14, the phase jumps originate from the sign changes of $\mathcal{B}(E_{\pm}, \theta)$ (near $\theta = 80^\circ$) and $\mathcal{D}(E_{\pm}, \theta)$ (near $\theta = 55^\circ$), which are determined by the competition between the s and d waves in pathways 1 and 2 (Fig. 6). Moreover, the location and the steepness of these phase jumps are determined by the specific values of the phases [Eq. (14)] and the coefficients [Eq. (17)] of the three 2ω -oscillation components in Eq. (16). Therefore, due to the different atomic phases of pathway 3 [Eq. (14c)] between the doublet P^h and P^l in each SB, i.e., $\varphi_L^{(3)}(E_+) \neq \varphi_L^{(3)}(E_-)$, the steepness of the phase jumps is different between P^h and P^l . In addition, the relative values of the coefficients are determined by the competition between pathways 1 and 3 (Fig. 4), which depends on the IR intensity and the photoelectron energy, thus the steepness of the phase jumps varies with the IR intensity and the photoelectron energy.

To compare these phase jumps more directly, we replot the RABBITT phases of the doublets P^h and P^l in SB 10 and SB 12 for the three IR intensities, as shown in Fig. 7. At each IR intensity, the phase jumps for P^h of SB 10 and SB 12 are more sharp than those for P^l . As the IR intensity increases, the phase jumps for P^h become more sharp while the phases for P^l undergo more gentle jumps. This IR-intensity dependence is traced back to the varying competition between pathways 1 and 3 (Fig. 4).

V. CONCLUSION

We have demonstrated the influence of Rabi oscillations on the phase of the emitted electron wave packet, utilizing the RABBITT technique by solving the 3D TDSE for lithium. In our scheme, the IR field induces the Rabi oscillations in

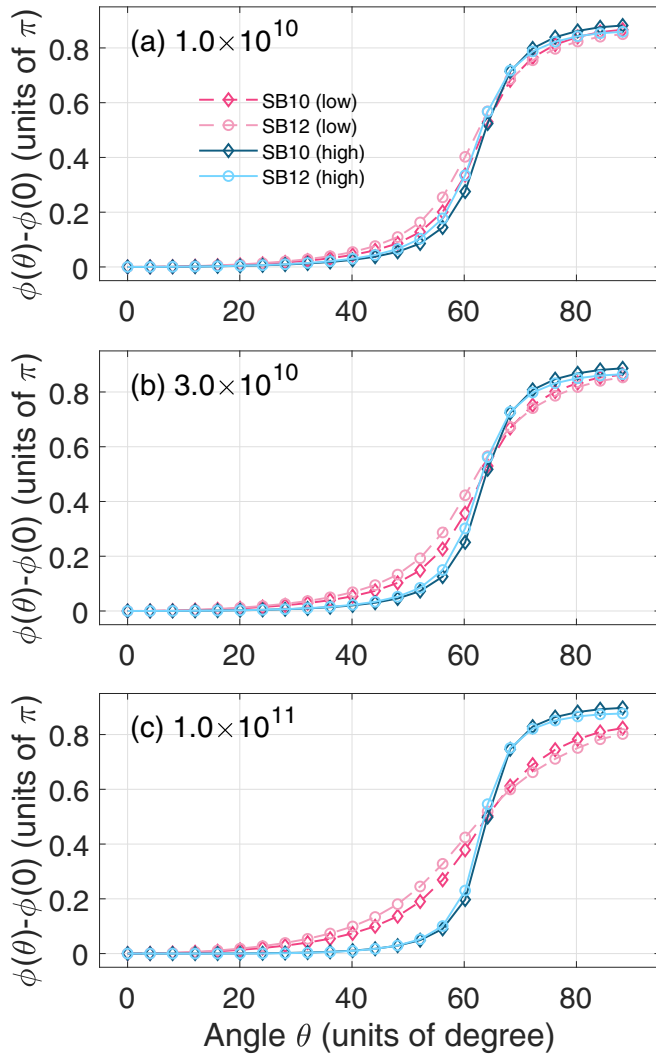


FIG. 7. The relative angle-resolved phases of P^l (dashed line) and P^h (solid line) in SB 10 (rhombuses) and SB 12 (circles) as a function of the emission angle of photoelectrons, for the IR intensities of (a) 1×10^{10} , (b) 3×10^{10} , and (c) 1×10^{11} W/cm².

the populations of the $2s$ and $2p$ states of lithium and AT splittings are resolvable in the photoelectron energy spectra by using the spectrally narrow laser fields. In the angle-integrated RABBITT measurement, the two signals of the doublet in each SB oscillate in different phases with the time delay between the XUV and IR fields and this relative phase varies with the photoelectron energy and the IR intensity. In the angle-resolved RABBITT measurement, the retrieved phases display rapid jumps as a function of the emission angle of photoelectrons, which originates from the interference among different continuum partial waves. The angle dependences of the RABBITT phases exhibit an obvious distinction between the two peaks of the doublet, the details of which depend on the photoelectron energy and the IR intensity. These different behaviors of the angle-integrated and angle-resolved phases stem from the unequal initial phases of the electron wave packets ionized from the dressed $2p$ states, which are further traced back to the out-of-phase oscillations in the $2p$ population with respect to the oscillations in the $2s$ population. Moreover, the details of the different phase behaviors between the two peaks of the doublet reveal the channel competition in the RABBITT process, which is sensitive to the photoelectron energy and the IR intensity. With the development of the spectral resolution in experiments, we believe these effects could be experimentally observed in the future.

ACKNOWLEDGMENTS

The authors acknowledge stimulating discussions with Prof. W.-C. Jiang, Prof. J. M. Dahlström, M. Bertolino, and E. Olofsson. This work was supported by National Key Research and Development Program of China (Grant No. 2019YFA0308300), National Natural Science Foundation of China (Grants No. 11874163, No. 12021004, and No. 61690222), and Chinese Academy of Sciences (Grants No. J20-021-III and No. S19-020-III). The computing work in this paper is supported by the Public Service Platform of High Performance Computing provided by Network and Computing Center of Huazhong University of Science and Technology (HUST).

- [1] M. Hentschel, R. Kienberger, C. Spielmann, G. A. Reider, N. Milosevic, T. Brabec, P. Corkum, U. Heinzmann, M. Drescher, and F. Krausz, *Nature (London)* **414**, 509 (2001).
- [2] P. M. Paul, E. S. Toma, P. Breger, G. Mullot, F. Augé, P. Balcou, H. G. Muller, and P. Agostini, *Science* **292**, 1689 (2001).
- [3] R. Pazourek, S. Nagele, and J. Burgdörfer, *Rev. Mod. Phys.* **87**, 765 (2015).
- [4] K. Klünder, J. M. Dahlström, M. Gisselbrecht, T. Fordell, M. Swoboda, D. Guénot, P. Johnsson, J. Caillat, J. Mauritsson, A. Maquet, R. Taïeb, and A. L'Huillier, *Phys. Rev. Lett.* **106**, 143002 (2011).
- [5] M. Isinger, R. J. Squibb, D. Busto, S. Zhong, A. Harth, D. Kroon, S. Nandi, C. L. Arnold, M. Miranda, J. M. Dahlström, E. Lindroth, R. Feifel, M. Gisselbrecht, and A. L'Huillier, *Science* **358**, 893 (2017).
- [6] C. Alexandridi, D. Platzer, L. Barreau, D. Busto, S. Zhong, M. Turconi, L. Neoričić, H. Laurell, C. L. Arnold, A. Borot, J.-F. Hergott, O. Tcherbakoff, M. Lejman, M. Gisselbrecht, E. Lindroth, A. L'Huillier, J. M. Dahlström, and P. Salières, *Phys. Rev. Research* **3**, L012012 (2021).
- [7] L. Cattaneo, J. Vos, R. Y. Bello, A. Palacios, S. Heuser, L. Pedrelli, M. Lucchini, C. Cirelli, F. Martín, and U. Keller, *Nat. Phys.* **14**, 733 (2018).
- [8] J. Vos, L. Cattaneo, S. Patchkovskii, T. Zimmermann, C. Cirelli, M. Lucchini, A. Kheifets, A. S. Landsman, and U. Keller, *Science* **360**, 1326 (2018).
- [9] S. Beaulieu, A. Comby, A. Clergerie, J. Caillat, D. Descamps, N. Dudovich, B. Fabre, R. Généaux, F. Lëgaré, S. Petit, B. Pons, G. Porat, T. Ruchon, R. Taïeb, V. Blanchet, and Y. Mairesse, *Science* **358**, 1288 (2017).
- [10] M. Lucchini, L. Castiglioni, L. Kasmi, P. Kliuiev, A. Ludwig, M. Greif, J. Osterwalder, M. Hengsberger, L. Gallmann, and U. Keller, *Phys. Rev. Lett.* **115**, 137401 (2015).

- [11] R. Locher, L. Castiglioni, M. Lucchini, M. Greif, L. Gallmann, J. Osterwalder, M. Hengsberger, and U. Keller, *Optica* **2**, 405 (2015).
- [12] I. Jordan, M. Huppert, D. Rattenbacher, M. Peper, D. Jelovina, C. Perry, A. von Conta, A. Schild, and H. J. Wörner, *Science* **369**, 974 (2020).
- [13] D. Baykusheva and H. J. Wörner, *J. Chem. Phys.* **146**, 124306 (2017).
- [14] M. Vacher, R. Gaillac, A. Maquet, R. Taïeb, and J. Caillat, *J. Opt.* **19**, 114011 (2017).
- [15] J. M. Dahlström, S. Pabst, and E. Lindroth, *APL Photonics* **4**, 011101 (2019).
- [16] S. Pabst and J. M. Dahlström, *Phys. Rev. A* **94**, 013411 (2016).
- [17] J. Fuchs, N. Douguet, S. Donsa, F. Martín, J. Burgdörfer, L. Argenti, L. Cattaneo, and U. Keller, *Phys. Rev. Research* **3**, 013195 (2021).
- [18] J. M. Dahlström, A. L'Huillier, and A. Maquet, *J. Phys. B* **45**, 183001 (2012).
- [19] J. Dahlström, D. Guénot, K. Klünder, M. Gisselbrecht, J. Mauritsson, A. L'Huillier, A. Maquet, and R. Taïeb, *Chem. Phys.* **414**, 53 (2013).
- [20] L. Argenti, A. Jiménez-Galán, J. Caillat, R. Taïeb, A. Maquet, and F. Martín, *Phys. Rev. A* **95**, 043426 (2017).
- [21] E. P. Wigner, *Phys. Rev.* **98**, 145 (1955).
- [22] F. T. Smith, *Phys. Rev.* **118**, 349 (1960).
- [23] D. Bharti, D. Atri-Schuller, G. Menning, K. R. Hamilton, R. Moshhammer, T. Pfeifer, N. Douguet, K. Bartschat, and A. Harth, *Phys. Rev. A* **103**, 022834 (2021).
- [24] J. Fuchs, N. Douguet, S. Donsa, F. Martín, J. Burgdörfer, L. Argenti, L. Cattaneo, and U. Keller, *Optica* **7**, 154 (2020).
- [25] J. Peschel, D. Busto, M. Plach, M. Bertolino, M. Hoflund, S. Maclot, J. Vinbladh, H. Wikmark, F. Zapata, E. Lindroth, M. Gisselbrecht, J. M. Dahlström, A. L'Huillier, and P. Eng-Johnsson, Complete characterization of multi-channel single photon ionization, [arXiv:2109.01581](https://arxiv.org/abs/2109.01581) (2021).
- [26] A. Jiménez-Galán, F. Martín, and L. Argenti, *Phys. Rev. A* **93**, 023429 (2016).
- [27] L. Barreau, C. L. M. Petersson, M. Klinker, A. Camper, C. Marante, T. Gorman, D. Kiesewetter, L. Argenti, P. Agostini, J. González-Vázquez, P. Salières, L. F. DiMauro, and F. Martín, *Phys. Rev. Lett.* **122**, 253203 (2019).
- [28] A. Jiménez-Galán, L. Argenti, and F. Martín, *Phys. Rev. Lett.* **113**, 263001 (2014).
- [29] U. Fano, *Phys. Rev.* **124**, 1866 (1961).
- [30] C. Cirelli, C. Marante, S. Heuser, C. L. M. Petersson, Á. J. Galán, L. Argenti, S. Zhong, D. Busto, M. Isinger, S. Nandi, S. Maclot, L. Rading, P. Johnsson, M. Gisselbrecht, M. Lucchini, L. Gallmann, J. M. Dahlström, E. Lindroth, A. L'Huillier, F. Martín, and U. Keller, *Nat. Commun.* **9**, 955 (2018).
- [31] V. Gruson, L. Barreau, Á. Jiménez-Galán, F. Risoud, J. Caillat, A. Maquet, B. Carré, F. Lepetit, J.-F. Hergott, T. Ruchon, L. Argenti, R. Taïeb, F. Martín, and P. Salières, *Science* **354**, 734 (2016).
- [32] M. Kotur, D. Guénot, Á. Jiménez-Galán, D. Kroon, E. W. Larsen, M. Louisy, S. Bengtsson, M. Miranda, J. Mauritsson, C. L. Arnold, S. E. Canton, M. Gisselbrecht, T. Carette, J. M. Dahlström, E. Lindroth, A. Maquet, L. Argenti, F. Martín, and A. L'Huillier, *Nat. Commun.* **7**, 10566 (2016).
- [33] S. Donsa, N. Douguet, J. Burgdörfer, I. Březinová, and L. Argenti, *Phys. Rev. Lett.* **123**, 133203 (2019).
- [34] M. Huppert, I. Jordan, D. Baykusheva, A. von Conta, and H. J. Wörner, *Phys. Rev. Lett.* **117**, 093001 (2016).
- [35] J. Caillat, A. Maquet, S. Haessler, B. Fabre, T. Ruchon, P. Salières, Y. Mairesse, and R. Taïeb, *Phys. Rev. Lett.* **106**, 093002 (2011).
- [36] S. Biswas, B. Förg, L. Ortmann, J. Schötz, W. Schweinberger, T. Zimmermann, L. Pi, D. Baykusheva, H. A. Masood, I. Lontos, A. M. Kamal, N. G. Kling, A. F. Alharbi, M. Alharbi, A. M. Azzeer, G. Hartmann, H. J. Wörner, A. S. Landsman, and M. F. Kling, *Nat. Phys.* **16**, 778 (2020).
- [37] L.-W. Pi and A. S. Landsman, *Appl. Sci.* **8**, 322 (2018).
- [38] S. Zhong, J. Vinbladh, D. Busto, R. J. Squibb, M. Isinger, L. Neoričić, H. Laurell, R. Weissenbilder, C. L. Arnold, R. Feifel, J. M. Dahlström, G. Wendin, M. Gisselbrecht, E. Lindroth, and A. L'Huillier, *Nat. Commun.* **11**, 5042 (2020).
- [39] M. Swoboda, T. Fordell, K. Klünder, J. M. Dahlström, M. Miranda, C. Buth, K. J. Schafer, J. Mauritsson, A. L'Huillier, and M. Gisselbrecht, *Phys. Rev. Lett.* **104**, 103003 (2010).
- [40] A. S. Kheifets and A. W. Bray, *Phys. Rev. A* **103**, L011101 (2021).
- [41] A. Kheifets, *Atoms* **9**, 66 (2021).
- [42] A. S. Kheifets, *Phys. Rev. A* **104**, L021103 (2021).
- [43] L. Drescher, T. Witting, O. Kornilov, and M. J. J. Vrakking, *Phys. Rev. A* **105**, L011101 (2022).
- [44] A. Autuori, D. Platzer, M. Lejman, G. Gallician, L. Maëder, A. Covolo, L. Bosse, M. Dalui, D. Bresteau, J.-F. Hergott, O. Tcherbakoff, H. J. B. Marroux, V. Lorient, F. Lépine, L. Poisson, R. Taïeb, J. Caillat, and P. Salières, *Sci. Adv.* **8**, eabl7594 (2022).
- [45] J. C. Baggesen and L. B. Madsen, *Phys. Rev. Lett.* **104**, 043602 (2010).
- [46] R. Pazourek, J. Feist, S. Nagele, and J. Burgdörfer, *Phys. Rev. Lett.* **108**, 163001 (2012).
- [47] M. Ossiander, F. Siegrist, V. Shirvanyan, R. Pazourek, A. Sommer, T. Latka, A. Guggenmos, S. Nagele, J. Feist, J. Burgdörfer, R. Kienberger, and M. Schultze, *Nat. Phys.* **13**, 280 (2017).
- [48] S. Donsa, M. Ederer, R. Pazourek, J. Burgdörfer, and I. Březinová, *Phys. Rev. A* **102**, 033112 (2020).
- [49] S. Heuser, A. Jiménez Galán, C. Cirelli, C. Marante, M. Sabbar, R. Boge, M. Lucchini, L. Gallmann, I. Ivanov, A. S. Kheifets, J. M. Dahlström, E. Lindroth, L. Argenti, F. Martín, and U. Keller, *Phys. Rev. A* **94**, 063409 (2016).
- [50] A. W. Bray, F. Naseem, and A. S. Kheifets, *Phys. Rev. A* **97**, 063404 (2018).
- [51] I. A. Ivanov and A. S. Kheifets, *Phys. Rev. A* **96**, 013408 (2017).
- [52] Q.-H. Ke, Y.-M. Zhou, Y.-J. Liao, J.-T. Liang, Y. Zhao, J. Tan, M. Li, and P.-X. Lu, *Front. Phys.* **16**, 52503 (2021).
- [53] C. Gerry and P. Knight, *Introductory Quantum Optics* (Cambridge University, New York, 2004).
- [54] S. H. Autler and C. H. Townes, *Phys. Rev.* **100**, 703 (1955).
- [55] J. Dalibard and C. Cohen-Tannoudji, *J. Opt. Soc. Am. B* **2**, 1707 (1985).
- [56] S. Nandi, E. Olofsson, M. Bertolino, S. Carlström, F. Zapata, D. Busto, C. Callegari, M. D. Fraia, P. Eng-Johnsson, R. Feifel, G. Gallician, M. Gisselbrecht, S. Maclot, L. Neoričić, J. Peschel, O. Plekan, K. C. Prince, R. J. Squibb, S. Zhong, P. V. Demekhin *et al.*, Studying ultrafast Rabi dynamics with a short-wavelength seeded free-electron laser, [arXiv:2201.10950](https://arxiv.org/abs/2201.10950) (2022).

- [57] A. Sarsa, F. Gálvez, and E. Buendía, *At. Data Nucl. Data Tables* **88**, 163 (2004).
- [58] T. N. Rescigno and C. W. McCurdy, *Phys. Rev. A* **62**, 032706 (2000).
- [59] W.-C. Jiang and X.-Q. Tian, *Opt. Express* **25**, 26832 (2017).
- [60] D. G. Arbó, J. E. Miraglia, M. S. Gravielle, K. Schiessl, E. Persson, and J. Burgdörfer, *Phys. Rev. A* **77**, 013401 (2008).
- [61] F. H. Faisal, *Theory of Multiphoton Processes* (Springer, New York, 1987).
- [62] F. C. Spano, *J. Chem. Phys.* **114**, 276 (2001).
- [63] W.-C. Jiang, H. Liang, S. Wang, L.-Y. Peng, and J. Burgdörfer, *Phys. Rev. Research* **3**, L032052 (2021).
- [64] C. J. Joachain, N. J. Kylstra, and R. M. Potvliege, *Atoms in Intense Laser Fields* (Cambridge University, New York, 2011).
- [65] R. W. Boyd, in *Nonlinear Optics*, 4th ed., edited by R. W. Boyd (Academic, New York, 2020), pp. 137–202.
- [66] A. Dalgarno, J. T. Lewis, and D. R. Bates, *Proc. R. Soc. A* **233**, 70 (1955).
- [67] L.-W. Pi and A. F. Starace, *Phys. Rev. A* **90**, 023403 (2014).
- [68] L.-W. Pi and A. F. Starace, *Phys. Rev. A* **82**, 053414 (2010).
- [69] M. Aymar and M. Crance, *J. Phys. B* **14**, 3585 (1981).
- [70] M. Marinescu, H. R. Sadeghpour, and A. Dalgarno, *J. Opt. Soc. Am. B* **10**, 988 (1993).
- [71] B. Gao and A. F. Starace, *Comput. Phys.* **1**, 70 (1987).
- [72] M. Dörr, O. Latinne, and C. J. Joachain, *Phys. Rev. A* **55**, 3697 (1997).
- [73] Y. Liao, Y. Zhou, L.-W. Pi, Q. Ke, J. Liang, Y. Zhao, M. Li, and P. Lu, *Phys. Rev. A* **104**, 013110 (2021).
- [74] L. Landau and E. Lifshitz, *Quantum Mechanics: Non-Relativistic Theory*, Course of Theoretical Physics (Elsevier, Amsterdam, 1991).
- [75] D. Busto, J. Vinbladh, S. Zhong, M. Isinger, S. Nandi, S. Maclot, P. Johnsson, M. Gisselbrecht, A. L’Huillier, E. Lindroth, and J. M. Dahlström, *Phys. Rev. Lett.* **123**, 133201 (2019).
- [76] M. Bertolino, D. Busto, F. Zapata, and J. M. Dahlström, *J. Phys. B* **53**, 144002 (2020).
- [77] U. Fano, *Phys. Rev. A* **32**, 617 (1985).